intramolecular mechanism is also feasible (Fig. 5a). We obtained strong evidence for a dissociative mechanism by measuring the rate of dimelamine exchange between assemblies $\mathbf{1}_3\cdot(\mathrm{BuCYA})_6$ and $\mathbf{2}_3\cdot(\mathrm{BuCYA})_6$ by ^{1}H NMR spectroscopy. Upon mixing these assemblies in a 1:1 ratio in benzene-d_6 at 70 °C, well-separated signals for the new heteromeric assemblies $\mathbf{1}_2\mathbf{2}_1\cdot(\mathrm{BuCYA})_6$ and $\mathbf{1}_1\mathbf{2}_2\cdot(\mathrm{BuCYA})_6$ appear over time as a result of the exchange of calix[4]arene dimelamines **1** and **2**. The rate-determining step in the exchange process involves the dissociation of calix[4]arene dimelamines from an intact assembly, a process that requires the disruption of a total of 12 hydrogen bonds. If racemization occurred via a dissociative mechanism, the rates of dimelamine exchange and racemization should be of similar magnitude. We studied the concentration dependence of the rate of dimelamine exchange, both with and without (*S*)-BAR present, and found that this rate can be expressed by the same equation as the rate of racemization, with slightly different values of k_{cat} and k_{uncat} ($14.7 \times 10^{-3}\,\mathrm{l\,mol^{-1}\,s^{-1}}$ and $7.0 \times 10^{-5}\,\mathrm{s^{-1}}$, respectively, at 70 °C). These values relate well to those obtained from the racemization studies. (The slightly higher values for dimelamine exchange are due to the slightly higher temperature at which these ^{1}H NMR experiments were conducted, 70 versus 50 °C). From these results we conclude that racemization occurs predominantly via a dissociative mechanism, both uncatalysed and catalysed (Fig. 5b and c). The rate-limiting step involves the dissociation of calix[4]arene dimelamines from the intact assembly, followed by rapid racemization and formation of the opposite enantiomer. □

Received 17 March; accepted 4 September 2000.

1. Lehn, J.-M. *Supramolecular Chemistry, Concepts and Perspectives* (VCH, Weinheim, 1995).
2. Whitesides, G. M. *et al.* Noncovalent synthesis: using physical-organic chemistry to make aggregates. *Acc. Chem. Res.* **28,** 37–44 (1995).
3. Piguet, C., Bernardinelli, G. & Hopfgartner, G. Helicates as versatile supramolecular complexes. *Chem. Rev.* **97,** 2005–2062 (1997)
4. Yashima, E., Maeda, K. & Okamoto, Y. Memory of macromolecular helicity assisted by interaction with achiral small molecules. *Nature* **399,** 449–451 (1999).
5. Furusho, Y., Kimura, T., Mizuno, Y. & Aida, T. Chirality-memory molecule: a D_2-symmetric fully substituted porphyrin as a conceptually new chirality sensor. *J. Am. Chem. Soc.* **119,** 5267–5268 (1997).
6. Prins, L. J., Huskens, J., De Jong, F., Timmerman, P. & Reinhoudt, D. N. Complete asymmetric induction of supramolecular chirality in a hydrogen-bonded assembly. *Nature* **398,** 498–502 (1999).
7. Suárez, M., Branda, N., Lehn, J.-M., Decian, A. & Fischer, J. Supramolecular chirality: chiral hydrogen-bonded supermolecules from achiral molecular components. *Helv. Chim. Acta* **81,** 1–13 (1998).
8. Rivera, J. M., Martin, T. & Rebek, J. Jr Chiral spaces: dissymmetric capsules through self-assembly. *Science* **279,** 1021–1023 (1998).
9. Castellano, R. K., Nuckolls, C. & Rebek, J. Jr Transfer of chiral information through molecular assembly. *J. Am. Chem. Soc.* **121,** 11156–11163 (1999).
10. Qiao, S., Choi, I. S. & Whitesides, G. M. Observation of diastereomers of the hydrogen-bonded aggregate $\mathrm{Hub(M)_3}$.3CA using ^{1}H NMR spectroscopy when CA is an optically-active isocyanuric acid. *J. Org. Chem.* **62,** 2619–2621 (1997).
11. Prins, L. J., Jolliffe, K. A., Hulst, R., Timmerman, P. & Reinhoudt, D. N. Control of structural isomerism in noncovalent hydrogen bonded assemblies using peripheral chiral information. *J. Am. Chem. Soc.* **122,** 3617–3627 (2000).
12. Vreekamp, R. H., Van Duynhoven, J. P. M., Hubert, M., Verboom, W. & Reinhoudt, D. N. Molecular boxes based on calix[4]arene double rosettes. *Angew. Chem. Int. Edn Engl.* **35,** 1215–1218 (1996).
13. Timmerman, P. *et al.* Noncovalent assembly of functional groups on calix[4]arene molecular boxes. *Chem. Eur. J.* **3,** 1823–1832 (1997).
14. Jolliffe, K. A. *et al.* Characterization of supramolecular hydrogen-bonded assemblies by MALDI-TOF mass spectrometry after Ag^+-labelling. *Angew. Chem. Int. Edn Engl.* **37,** 1294–1297 (1998).
15. Mascal, M. *et al.* The ion-pair reinforced, hydrogen-bonding molecular ribbon. *J. Chem. Soc. Chem. Commun.* 805–806 (1995).
16. Shieh, H. S. & Voet, D. The x-ray structure of the molecular complex 8-bromo-9-ethyladenine-cyanuric acid monohydrate. *Acta Crystallogr. B* **32,** 2354–2360 (1976).
17. Yashima, E., Matsushima, T. & Okamoto, Y. Chirality assignment of amines and amino alcohols based on circular dichroism induced by helix formation of a stereoregular poly((4-carboxyphenyl)acetylene) through acid-base complexation. *J. Am. Chem. Soc.* **119,** 6345–6359 (1997).
18. Palmans, A. R. A., Vekemans, J. A. J. M., Havinga, E. E. & Meijer, E. W. Sergeants-and-soldiers principle in chiral columnar stacks of disc-shaped molecules with C_3 symmetry. *Angew. Chem. Int. Edn Engl.* **36,** 2648–2651 (1997).
19. Green, M. M. *et al.* A helical polymer with a cooperative response to chiral information. *Science* **268,** 1860–1866 (1995).

Supplementary Information is available on *Nature*'s World-Wide Web site (http://www.nature.com) or as paper copy from the London editorial office of *Nature*.

Acknowledgements

We thank C. Marjo and A. Bielejewska for their work on the model complexes **4·5** and **4·6**, and R. Fokkens and N.M.M. Nibbering for the MALDI-TOF MS measurements. This work was supported by the Council for Chemical Sciences of the Netherlands Organization for Scientific Research (CW-NWO).

Correspondence and requests for materials should be addressed to D.N.R. (e-mail: smct@ct.utwente.nl).

Acceleration of global warming due to carbon-cycle feedbacks in a coupled climate model

Peter M. Cox*, Richard A. Betts*, Chris D. Jones*, Steven A. Spall* & Ian J. Totterdell†

* *Hadley Centre, The Met Office, Bracknell, Berkshire RG12 2SY, UK*
† *Southampton Oceanography Centre, European Way, Southampton SO14 3ZH, UK*

The continued increase in the atmospheric concentration of carbon dioxide due to anthropogenic emissions is predicted to lead to significant changes in climate[1]. About half of the current emissions are being absorbed by the ocean and by land ecosystems[2], but this absorption is sensitive to climate[3,4] as well as to atmospheric carbon dioxide concentrations[5], creating a feedback loop. General circulation models have generally excluded the feedback between climate and the biosphere, using static vegetation distributions and CO_2 concentrations from simple carbon-cycle models that do not include climate change[6]. Here we present results from a fully coupled, three-dimensional carbon–climate model, indicating that carbon-cycle feedbacks could significantly accelerate climate change over the twenty-first century. We find that under a 'business as usual' scenario, the terrestrial biosphere acts as an overall carbon sink until about 2050, but turns into a source thereafter. By 2100, the ocean uptake rate of 5 Gt C yr^{-1} is balanced by the terrestrial carbon source, and atmospheric CO_2 concentrations are 250 p.p.m.v. higher in our fully coupled simulation than in uncoupled carbon models[2], resulting in a global-mean warming of 5.5 K, as compared to 4 K without the carbon-cycle feedback.

The general circulation model (GCM) that we used is based on the third Hadley Centre coupled ocean–atmosphere model, HadCM3[7], which we have coupled to an ocean carbon-cycle model (HadOCC) and a dynamic global vegetation model (TRIFFID). The atmospheric physics and dynamics of our GCM are identical to those used in HadCM3, but the additional computational expense of including an interactive carbon cycle made it necessary to reduce the ocean resolution to 2.5° × 3.75°, necessitating the use of flux adjustments in the ocean component to counteract climate drift. HadOCC accounts for the atmosphere–ocean exchange of CO_2, and the transfer of CO_2 to depth through both the solubility pump and the biological pump[8]. TRIFFID models the state of the biosphere in terms of the soil carbon, and the structure and coverage of five functional types of plant within each model gridbox (broadleaf tree, needleleaf tree, C_3 grass, C_4 grass and shrub). Further details on HadOCC and TRIFFID are given in Methods.

The coupled climate/carbon-cycle model was brought to equilibrium with a 'pre-industrial' atmospheric CO_2 concentration of 290 p.p.m.v., starting from an observed landcover data set[9]. The resulting state was stable, with negligible net land–atmosphere and

ocean–atmosphere carbon fluxes in the long-term mean, and no discernible drift in atmospheric CO_2 concentration. This simulation produces the locations of the main land biomes, and estimates of ocean carbon (38,100 Gt C), vegetation carbon (493 Gt C), soil carbon (1,180 Gt C) and terrestrial net primary productivity (60 Gt C yr^{-1}) that are within the range of other estimates[2,10–12]. Ocean primary productivity is also compatible with results derived from remote sensing[13,14], producing a global-mean total of 53 Gt C yr^{-1}, and realistic seasonal and latitudinal variations[15].

The simulated carbon cycle displays significant interannual variability, which is driven by the model-generated El Niño/Southern Oscillation (ENSO). A realistic response to internal climate variability is an important prerequisite for any carbon-cycle model to be used in climate change predictions. Fluctuations in annual-mean atmospheric CO_2 are correlated with the phase of ENSO, as indicated by the Nino3 index (Fig. 1). During El Niño conditions (positive Nino3), the model simulates an increase in atmospheric CO_2; this increase results from the terrestrial biosphere acting as a large source (especially in Amazonia[16]), which is only partially offset by a reduced outgassing from the tropical Pacific Ocean. The opposite is true during the La Niña phase. The overall sensitivity of the modelled carbon cycle to ENSO variability is consistent with the observational record[17], demonstrating that the coupled system responds realistically to climate anomalies.

Transient simulations were carried out for 1860–2100, using CO_2 emissions as given by the IS92a scenario[18]. Other greenhouse gases were also prescribed from IS92a, but the radiative effects of sulphate aerosols were omitted. Three separate runs were completed to isolate the effect of climate/carbon-cycle feedbacks; an experiment with prescribed IS92a CO_2 and fixed vegetation (that is, a 'standard' GCM climate change simulation), an experiment with interactive CO_2 and dynamic vegetation but no direct effects of CO_2 on climate (akin to 'offline' carbon-cycle projections that neglect climate change[6]), and a fully coupled climate/carbon-cycle simulation.

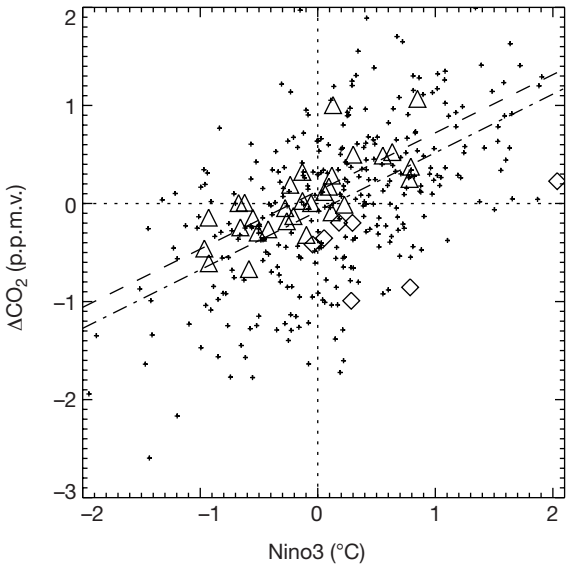

Figure 1 Modelled and observed interannual variability in the atmospheric CO_2 concentration. The figure shows the anomaly in the growth rate of atmospheric CO_2 versus the Nino3 index, taken from our pre-industrial control simulation (crosses) and the Mauna Loa observations (triangles). (The Nino3 index is the annual mean sea surface temperature anomaly in the tropical Pacific, 150° W–90° W, 5° S–5° N.) The gradients of the dashed and dot-dashed lines represent the sensitivity of the carbon cycle to ENSO, as given by the observations and the model, respectively. We have excluded observations that immediately follow major volcanic events (data points shown by diamonds), since during these years the carbon cycle may have been significantly perturbed by the induced tropospheric cooling.

Figure 2 shows results from the fully coupled run. From 1860 to 2000, the simulated stores of carbon in the ocean and on land increase by about 100 Gt C and 75 Gt C, respectively. However, the atmospheric CO_2 is 15–20 p.p.m.v. too high by the present day (corresponding to a timing error of about 10 years). Possible reasons for this include an overestimate of the prescribed net land-use emissions and the absence of other important climate forcing factors. The modelled global mean temperature increase from 1860 to 2000 is about 1.4 K (Fig. 3b), which is higher than observed[19], probably due to the absence of cooling from anthropogenic aerosols[20]. Offline tests suggest that such a relative warming can suppress the terrestrial carbon sink by enhancing soil and plant respiration[11]. Nevertheless, the rate of increase of CO_2 from 1950 to 2000 closely follows the recent observational record, which implies that the airborne fraction is being well simulated over this period. For the 20 years centred on 1985, the mean land and ocean uptake of carbon are 1.5 and 1.6 Gt yr^{-1}, respectively (compare best estimates for the 1980s of 1.8 ± 1.8 and 2.0 ± 0.8 Gt yr^{-1})[2]. The model therefore captures the most important characteristics of the present-day carbon cycle.

The simulated atmospheric CO_2 diverges much more rapidly from the standard IS92a concentration scenario in the future. First, vegetation carbon in South America begins to decline, as a drying and warming of Amazonia initiates loss of forest (Fig. 4a). This is driven purely by climate change, as can be seen by comparing the fully coupled run (red lines) to the run without global warming (blue lines). The effects of anthropogenic deforestation on land-cover are neglected in both cases. A second critical point is reached at about 2050, when the land biosphere as a whole switches from being a weak sink for CO_2 to being a strong source (Fig. 2). The reduction in terrestrial carbon from around 2050 onward is associated with a widespread climate-driven loss of soil carbon (Fig. 4b). An increase in the concentration of atmospheric CO_2 alone tends to increase the rate of photosynthesis and thus terrestrial carbon storage, provided that other resources are not limiting[4]. However, plant maintenance and soil respiration rates both increase with temperature. As a consequence, climate warming (the indirect effect of a CO_2 increase) tends to reduce terrestrial carbon storage[11], especially in the warmer regions where an increase in temperature is

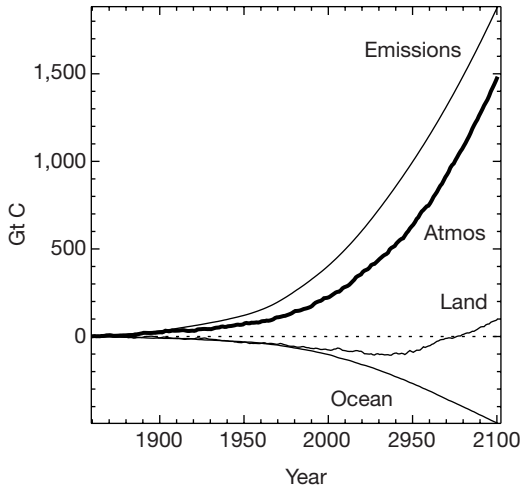

Figure 2 Budgets of carbon during the fully coupled simulation. The thick line shows the simulated change in atmospheric CO_2. The thinner lines show the integrated impact of the emissions, and of land and ocean fluxes, on the atmospheric CO_2 increase, with negative values implying net uptake of CO_2. We note that the terrestrial biosphere takes up CO_2 at a decreasing rate from about 2010 onwards, becoming a net source at around 2050. By 2100 this source from the land almost balances the oceanic sink, so that atmospheric carbon content is increasing at about the same rate as the integrated emissions (that is, the airborne fraction is ~1).

not beneficial for photosynthesis. At low CO_2 concentrations the direct effect of CO_2 dominates, and both vegetation and soil carbon increase with atmospheric CO_2. But as CO_2 increases further, terrestrial carbon begins to decrease, because the direct effect of CO_2 on photosynthesis saturates but the specific soil respiration rate continues to increase with temperature. The transition between these two regimes occurs abruptly at around 2050 in this experiment (Fig. 4b). The carbon stored on land decreases by about 170 Gt C from 2000 to 2100, accelerating the rate of atmospheric CO_2 increase over this period.

The ocean takes up about 400 Gt C over the same period, but at a rate which is asymptotically approaching 5 Gt C yr^{-1} by 2100. This reduced efficiency of oceanic uptake is partly a consequence of the nonlinear dependence of the partial pressure of dissolved CO_2 on the total ocean carbon concentration, but may also have contributions from climate change[3]. Although the thermohaline circulation of the ocean weakens[21] by about 25% from 2000 to 2100, this is much less of a reduction than seen in some previous simulations[22], and the corresponding effect on ocean carbon uptake is less significant. In our experiment, increased thermal stratification due to warming of the sea surface suppresses upwelling, which reduces nutrient availability and lowers primary production by about 5%. However, ocean-only tests suggest a small effect of climate change on oceanic carbon uptake, as this reduction in the biological pump is compensated by reduced upwelling of deep waters which have high concentrations of total carbon.

By 2100 the modelled CO_2 concentration is about 980 p.p.m.v. in the coupled experiment, which is more than 250 p.p.m.v. higher than the standard IS92a scenario or that simulated in the 'offline' experiment (Fig. 3a). As a result, the global-mean land temperatures increase from 1860 to 2100 by about 8 K, rather than the 5.5 K of the standard scenario (Fig. 3b).

These numerical experiments demonstrate the potential importance of climate/carbon-cycle feedbacks, but the magnitude of these in the real Earth system is still highly uncertain. Terrestrial carbon models differ in their responses to climate change[11,12], owing to gaps in basic understanding of processes. For example, the potential conversion of the global terrestrial carbon sink to a source is critically dependent upon the long-term sensitivity of soil respiration to global warming, which is still a subject of debate[23]. The experiments presented here exclude the potentially large direct human influences on terrestrial carbon uptake through changes in landcover and land management. Local effects, such as the possible climate-driven loss of the Amazon rainforest, rest upon uncertain aspects of regional climate change, and may be 'short-circuited' by direct human deforestation. A full assessment of the uncertainties must await further coupled experiments utilizing alternative representations of processes and including a more complete set of natural

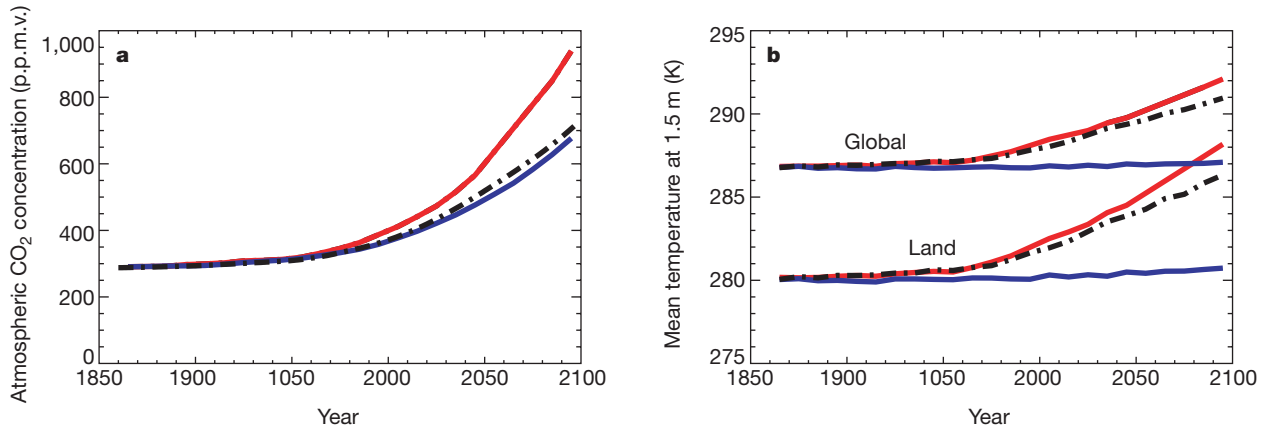

Figure 3 Effect of climate/carbon-cycle feedbacks on CO_2 increase and global warming. **a**, Global-mean CO_2 concentration, and **b**, global-mean and land-mean temperature, versus year. Three simulations are shown; the fully coupled simulation with interactive CO_2 and dynamic vegetation (red lines), a standard GCM climate change simulation with prescribed (IS92a) CO_2 concentration and fixed vegetation (dot-dashed lines), and the simulation which neglects direct CO_2-induced climate change (blue lines). The slight warming in the latter is due to CO_2-induced changes in stomatal conductance and vegetation distribution.

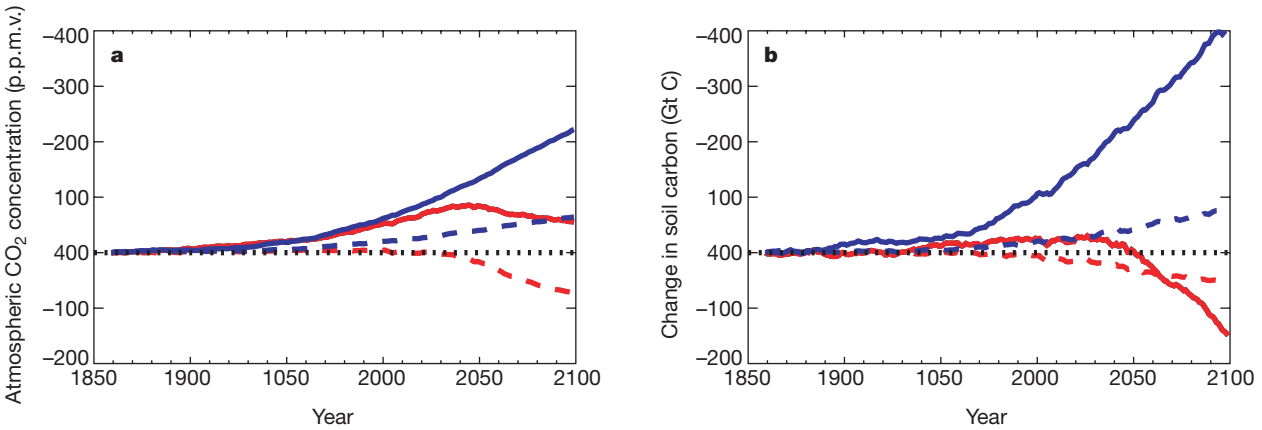

Figure 4 Effect of global warming on changes in land carbon storage. The red lines represent the fully coupled climate/carbon-cycle simulation, and the blue lines are from the 'offline' simulation which neglects direct CO_2-induced climate change. The figure shows simulated changes in vegetation carbon (**a**) and soil carbon (**b**) for the global land area (continuous lines) and South America alone (dashed lines).

and anthropogenic forcing factors (for example, land-use change, forest fires, sulphate aerosol concentrations and nitrogen deposition). However, our results indicate that it will be essential to accurately represent previously neglected carbon-cycle feedbacks if we are to successfully predict climate change over the next 100 years. □

Methods

Ocean carbon-cycle model

The inorganic component of HadOCC has been extensively tested as part of the Ocean Carbon Cycle Intercomparison Project; it was found to reproduce tracer distributions to an accuracy consistent with other ocean GCMs[24]. The biological component treats four additional ocean fields: nutrient, phytoplankton, zooplankton and detritus[8]. The phytoplankton population changes as a result of the balance between growth, which is controlled by light level and the local concentration of nutrient, and mortality, which is mostly as a result of grazing by zooplankton. Detritus, which is formed by zooplankton excretion and by phyto- and zooplankton mortality, sinks at a fixed rate and slowly remineralizes to reform nutrient and dissolved inorganic carbon. Thus both nutrient and carbon are absorbed by phytoplankton near the ocean surface, pass up the food chain to zooplankton, and are eventually remineralized from detritus in the deeper ocean. The model also includes the formation of calcium carbonate and its dissolution at depth (below the lysocline).

Terrestrial carbon-cycle model

TRIFFID (top-down representation of interactive foliage and flora including dynamics) has been used offline in a comparison of dynamic global vegetation models[11]. Carbon fluxes for each vegetation type are calculated every 30 minutes as a function of climate and atmospheric CO_2 concentration, from a coupled photosynthesis/stomatal-conductance scheme[25,26], which utilizes existing models of leaf-level photosynthesis in C_3 and C_4 plants[27,28]. The accumulated fluxes are used to update the vegetation and soil carbon every 10 days. The natural landcover evolves dynamically based on competition between the vegetation types, which is modelled using a Lotka–Volterra approach and a tree–shrub–grass dominance hierarchy. We also prescribe some agricultural regions, in which grasslands are assumed to be dominant. Carbon lost from the vegetation as a result of local litterfall or large-scale disturbance is transferred into a soil carbon pool, where it is broken down by microorganisms that return CO_2 to the atmosphere. The soil respiration rate is assumed to double for every 10 K of warming[29], and is also dependent on the soil moisture content[30]. Changes in the biophysical properties of the land surface[5], as well as changes in terrestrial carbon, feed back onto the atmosphere.

Received 6 January; accepted 26 September 2000.

1. Houghton, J. T. *et al.* (eds) *Climate Change 1995: The Science of Climate Change* (Cambridge Univ. Press, Cambridge, 1996).
2. Schimel, D. *et al.* in *Climate Change 1995: The Science of Climate Change* Ch. 2 (eds Houghton, J. T. *et al.*) 65–131 (Cambridge Univ. Press, Cambridge, 1995).
3. Sarmiento, J., Hughes, T., Stouffer, R. & Manabe, S. Simulated response of the ocean carbon cycle to anthropogenic climate warming. *Nature* **393,** 245–249 (1998).
4. Cao, M. & Woodward, F. I. Dynamic responses of terrestrial ecosystem carbon cycling to global climate change. *Nature* **393,** 249–252 (1998).
5. Betts, R. A., Cox, P. M., Lee, S. E. & Woodward, F. I. Contrasting physiological and structural vegetation feedbacks in climate change simulations. *Nature* **387,** 796–799 (1997).
6. Enting, I., Wigley, T. & Heimann, M. *Future Emissions and Concentrations of Carbon Dioxide; Key Ocean/Atmosphere/Land Analyses* (Technical Paper 31, Division of Atmospheric Research, CSIRO, Melbourne, 1994).
7. Gordon, C. *et al.* The simulation of SST, sea ice extents and ocean heat transports in a version of the Hadley Centre coupled model without flux adjustments. *Clim. Dyn.* **16,** 147–168 (2000).
8. Palmer, J. R. & Totterdell, I. J. Production and export in a global ocean ecosystem model. *Deep-Sea Res.* (in the press).
9. Wilson, M. F. & Henderson-Sellers, A. A global archive of land cover and soils data for use in general circulation climate models. *J. Clim.* **5,** 119–143 (1985).
10. Zinke, P. J., Stangenberger, A. G., Post, W. M., Emanuel, W. R. & Olson, J. S. *Worldwide Organic Soil Carbon and Nitrogen Data* (NDP-018, Carbon Dioxide Information Center, Oak Ridge National Laboratory, Oak Ridge, Tennessee, 1986).
11. Cramer, W. *et al.* Global response of terrestrial ecosystem structure and function to CO_2 and climate change: results from six dynamic global vegetation models. *Glob. Change Biol.* (in the press).
12. VEMAP Members. Vegetation/ecosystem modelling and analysis project: comparing biogeography and biogeochemistry models in a continental-scale study of terrestrial responses to climate change and CO_2 doubling. *Glob. Biogeochem. Cycles* **9,** 407–437 (1995).
13. Longhurst, A., Sathyendranath, S., Platt, T. & Caverhill, C. An estimate of global primary production in the ocean from satellite radiometer data. *J. Plank. Res.* **17,** 1245–1271 (1995).
14. Field, C., Behrenfeld, M., Randerson, J. & Falkowski, P. Primary production of the biosphere: integrating terrestrial and oceanic components. *Science* **281,** 237–240 (1998).
15. Antoine, D., Andre, J.-M. & Morel, A. Oceanic primary production 2. Estimation at global scale from satellite (Coastal Zone Color Scanner) chlorophyll. *Glob. Biogeochem. Cycles* **10,** 57–69 (1996).
16. Tian, H. *et al.* Effects of interannual climate variability on carbon storage in Amazonian ecosystems. *Nature* **396,** 664–667 (1998).
17. Keeling, C. D., Whorf, T., Whalen, M. & der Plicht, J. V. Interannual extremes in the rate of rise of atmospheric carbon dioxide since 1980. *Nature* **375,** 666–670 (1995).
18. Houghton, J. T., Callander, B. A. & Varney, S. K. (eds) *Climate Change 1992: The Supplementary Report to the IPCC Scientific Assessment* (Cambridge Univ. Press, Cambridge, 1992).
19. Nicholls, N. *et al.* in *Climate Change 1995: The Science of Climate Change* Ch. 3 (eds Houghton, J. T. *et al.*) (Cambridge Univ. Press, Cambridge, 1996).
20. Mitchell, J. F. B., Johns, T. C., Gregory, J. M. & Tett, S. F. B. Climate response to increasing levels of greenhouse gases and sulphate aerosols. *Nature* **376,** 501–504 (1995).
21. Wood, R. A., Keen, A. B., Mitchell, J. F. B. & Gregory, J. M. Changing spatial structure of the thermohaline circulation in response to atmospheric CO_2 forcing in a climate model. *Nature* **399,** 572–575 (1999).
22. Sarmiento, J. & Quere, C. L. Oceanic carbon dioxide uptake in a model of century-scale global warming. *Nature* **274,** 1346–1350 (1996).
23. Giardina, C. & Ryan, M. Evidence that decomposition rates of organic carbon in mineral soil do not vary with temperature. *Nature* **404,** 858–861 (2000).
24. Orr, J. C. in *Ocean Storage of Carbon Dioxide, Workshop 3: International Links and Concerns* (ed. Ormerod, W.) 33–52 (IEA R&D Programme, CRE Group Ltd, Cheltenham, UK, 1996).
25. Cox, P. M., Huntingford, C. & Harding, R. J. A canopy conductance and photosynthesis model for use in a GCM land surface scheme. *J. Hydrol.* **212–213,** 79–94 (1998).
26. Cox, P. M. *et al.* The impact of new land surface physics on the GCM simulation of climate and climate sensitivity. *Clim. Dyn.* **15,** 183–203 (1999).
27. Collatz, G. J., Ball, J. T., Grivet, C. & Berry, J. A. Physiological and environmental regulation of stomatal conductance, photosynthesis and transpiration: a model that includes a laminar boundary layer. *Agric. Forest Meteorol.* **54,** 107–136 (1991).
28. Collatz, G. J., Ribas-Carbo, M. & Berry, J. A. A coupled photosynthesis-stomatal conductance model for leaves of C4 plants. *Aust. J. Plant Physiol.* **19,** 519–538 (1992).
29. Raich, J. & Schlesinger, W. The global carbon dioxide flux in soil respiration and its relationship to vegetation and climate. *Tellus B* **44,** 81–99 (1992).
30. McGuire, A. *et al.* Interactions between carbon and nitrogen dynamics in estimating net primary productivity for potential vegetation in North America. *Glob. Biogeochem. Cycles* **6,** 101–124 (1992).

Acknowledgements

We thank J. Mitchell and G. Jenkins for comments on earlier versions of the manuscript. This work was supported by the UK Department of the Environment, Transport and the Regions.

Correspondence and requests for materials should be addressed to P.M.C. (e-mail: pmcox@meto.gov.uk).

Offset of the potential carbon sink from boreal forestation by decreases in surface albedo

Richard A. Betts

Hadley Centre for Climate Prediction and Research, The Met Office, Bracknell, Berkshire RG12 2SY, UK

Carbon uptake by forestation is one method proposed[1] to reduce net carbon dioxide emissions to the atmosphere and so limit the radiative forcing of climate change[2]. But the overall impact of forestation on climate will also depend on other effects associated with the creation of new forests. In particular, the albedo of a forested landscape is generally lower than that of cultivated land, especially when snow is lying[3–9], and decreasing albedo exerts a positive radiative forcing on climate. Here I simulate the radiative forcings associated with changes in surface albedo as a result of forestation in temperate and boreal forest areas, and translate these forcings into equivalent changes in local carbon stock for comparison with estimated carbon sequestration potentials[10–12]. I suggest that in many boreal forest areas, the positive forcing induced by decreases in albedo can offset the negative forcing that is expected from carbon sequestration. Some high-latitude forestation activities may therefore increase climate change, rather than mitigating it as intended.

Perturbations to the balance between radiation absorbed and emitted by the Earth ('radiative forcing') can result from changes in atmospheric chemistry and planetary albedo. A positive 'greenhouse' forcing results from increased atmospheric CO_2 absorbing and re-emitting more of the infrared radiation emitted by the surface[13]; forestation may help to mitigate this by slowing the rise